Publ. Astron. Soc. Japan (2014) 00(0), 1–14
doi: 10.1093/pasj/xxx000

arXiv:1608.07284v1 [astro-ph.GA] 25 Aug 2016

X-ray and infrared diagnostics of nearby active galactic nuclei with MAXI and AKARI.

Naoki ISOBE [1,2], Taiki KAWAMURO [3], Shinki OYABU [4], Takao NAKAGAWA [2], Shunsuke BABA [2,5], Kenichi YANO [2,5], Yoshihiro UEDA [3], & Yoshiki TOBA [6,7]

[1] School of Science, Tokyo Institute of Technology, 2-12-1 Ookayama, Meguro, Tokyo 152-8551, Japan
[2] Institute of Space and Astronautical Science (ISAS), Japan Aerospace Exploration Agency (JAXA), 3-1-1 Yoshinodai, Chuo-ku, Sagamihara, Kanagawa 252-5210, Japan
[3] Department of Astronomy, Kyoto University, Oiwake-cho, Sakyo-ku, Kyoto 606-8502, Japan
[4] Graduate School of Science, Nagoya University, Furo-cho, Chikusa-ku, Nagoya, Aichi 464-8602, Japan
[5] Department of Physics, The University of Tokyo, 7-3-1, Hongo, Bunkyo-ku, Tokyo, 133-0033, Japan
[6] Research Center for Space and Cosmic Evolution, Ehime University, 2-5 Bunkyo-cho, Matsuyama, Ehime 790-8577, Japan
[7] Academia Sinica Institute of Astronomy and Astrophysics, PO Box 23-141, Taipei 10617, Taiwan

*E-mail: n-isobe@hp.phys.titech.ac.jp

Received 2016 June 20; Accepted 2016 August 23

Abstract

Nearby active galactic nuclei were diagnosed in the X-ray and mid-to-far infrared wavelengths, with Monitor of All-sky X-ray Image (MAXI) and the Japanese infrared observatory AKARI, respectively. Among the X-ray sources listed in the second release of the MAXI all-sky X-ray source catalog, 100 ones are currently identified as a non-blazar-type active galactic nucleus. These include 95 Seyfert galaxies and 5 quasars, and they are composed of 73 type-1 and 27 type-2 objects. The AKARI all-sky survey point source catalog was searched for their mid- and far-infrared counterparts at 9, 18, and 90 μm. As a result, 69 Seyfert galaxies in the MAXI catalog (48 type-1 and 21 type-2 ones) were found to be detected with AKARI. The X-ray (3–4 keV and 4–10 keV) and infrared luminosities of these objects were investigated, together with their color information. Adopting the canonical photon index, $\Gamma = 1.9$, of the intrinsic X-ray spectrum of the Seyfert galaxies, the X-ray hardness ratio between the 3–4 and 4–10 keV ranges derived with MAXI was roughly converted into the absorption column density. After the X-ray luminosity was corrected for absorption from the estimated column density, the well-known X-ray-to-infrared luminosity correlation was confirmed at least in the Compton-thin regime. In contrast, NGC 1365, only one Compton-thick object in the MAXI catalog, was found to deviate from the correlation toward a significantly lower X-ray luminosity by nearly an order of magnitude. It was verified that the relation between the X-ray hardness below 10 keV and X-ray-to-infrared color acts as an effective tool to pick up Compton-thick objects. The difference in the infrared colors between the type-1 and type-2 Seyfert galaxies and its physical implication on the classification and unification of active galactic nuclei were briefly discussed.

© 2014. Astronomical Society of Japan.

Key words: galaxies: active — galaxies: Seyfert — X-rays: galaxies — infrared: galaxies

1 Introduction

The unified picture of active galactic nuclei (e.g., Antonucci 1993; Urry & Padovani 1995) invokes a supermassive black hole accompanied by a mass accreting disk as their central engine. It is widely believed that they are surrounded by a parsec-scale torus filled with dust and gas clouds. However, the detailed physical condition and spatial configuration of these essential ingredients in the active galactic nuclei still remain one of the important issues yet to be solved in the modern astrophysics.

The active galactic nuclei are widely known as an X-ray emitter. Except for jet-dominated sources including blazars and BL Lacertae objects, their X-ray emission is thought to originate in a hot corona above the accretion disk, where disk photons are Comptonized (e.g., Sunyaev & Titarchuk 1980). After the nuclear radiation is absorbed by the dust torus, it is re-emitted into the mid-to-far infrared (IR) wavelength. As a result, the active galactic nuclei, without any significant jet contamination, typically exhibit a strong IR bump in their spectral energy distribution around 1 – 100 μm (e.g., Sanders et al. 1989; Antonucci 1993; Elvis et al. 1994; Elitzur 2008). These properties make a combination of X-ray and IR observations an ideal probe for the central region of the active galactic nuclei. Actually, a number of recent studies indicate a linear correlation between the absorption-corrected (or -unaffected) X-ray luminosities and the observed IR ones among nearby active galactic nuclei with a moderate absorbing Hydrogen column density of $N_{\rm H} \lesssim 10^{24}$ cm^{-2}, regardless of their optical classification (Gandhi et al. 2009; Matsuta et al. 2012; Ichikawa et al. 2012). Such a correlation is supposed to prefer a so-called clumpy torus geometry (e.g., Krolik & Begelman 1988), instead of a simple torus model with a smooth and homogeneous dust distribution (e.g., Pier & Krolik 1993), because the latter model requests a deficit in the observed IR luminosity from obscured objects due to self-extinction within the dust torus.

Owing to tremendous progress in multi-wavelength observations, active galactic nuclei that are deeply enshrouded by the dust (e.g., Ueda et al. 2007) have gradually been uncovered. Among such heavily obscured active galactic nuclei, those with $N_{\rm H} > 1.5 \times 10^{24}$ cm^{-2} are widely called as Compton-thick objects. In spite of their astrophysical importance for various reasons, such as the origin of the X-ray background radiation (Gilli et al. 2007; Ueda et al. 2014), the Compton-thick sources are rather elusive in optical observations because of severe dust extinction. Even hard X-ray surveys performed with the Burst Alert Telescope (BAT) onboard the Swift observatory is inferred to have eventually undercounted the Compton-thick objects by a factor of ~ 4 (Burlon et al. 2011), although hard X-ray photons above 10 keV are expected to exhibit a high penetrating power. In contrast, it is recently proposed that a combination of X-ray and IR color information is very useful to select the heavily obscured population (Severgnini et al. 2015; Terashima et al. 2015).

Previous unbiased X-ray and IR diagnostics on nearby active galactic nuclei are usually based on the hard X-ray survey above 10 keV (Matsuta et al. 2012; Ichikawa et al. 2012). In contrast, the 2–10 keV X-ray spectral information, obtained with recent X-ray telescopes, such as Suzaku (Mitsuda et al. 2007), Chandra, and XMM-Newton, is one of the most standard and powerful tools to investigate the properties of active galaxies. It is important to compare results from the detailed spectral analysis with those from all-sky X-ray surveys in the same energy range, namely below 10 keV. However, the 2–10 keV samples of active galactic nuclei adopted for the X-ray-to-IR studies were frequently constructed from a restricted sky field (e.g., Gandhi et al. 2009). Therefore, unbiased all-sky survey data below 10 keV with a high sensitivity has been strongly requested.

In the present study, we overcome such situation, by making use of the X-ray source catalog with the Monitor of All-sky X-ray Image (MAXI; Matsuoka et al. 2009) and the IR one with the Japanese space IR observatory AKARI (Murakami et al. 2007). MAXI has continuously monitored all the X-ray sky below 10 keV with the sensitivity higher than any other previous all-sky X-ray survey missions. In the second release of the MAXI all-sky X-ray source catalog (hereafter the 2MAXI catalog; Hiroi et al. 2013), more than 100 active galactic nuclei, including Seyfert galaxies, quasars and blazars, are listed. Considering the size of the dust torus (typically a parsec scale, corresponding to the light-crossing time of a few years), the X-ray flux averaged over ~ 3 years, which is provide by the 2MAXI catalog, is valuable rather than snap-shot data obtained with the pointing X-ray satellites. The hardness ratio within the MAXI energy range is regarded as a good indicator of the absorption column density of the dust torus. The ability of MAXI for studies of active galactic nuclei was demonstrated by several authors (e.g., Isobe et al. 2010; Isobe et al. 2015; Tachibana et al. 2016).

The IR characteristics of the active galactic nuclei, picked up from the 2MAXI catalog, were examined with the AKARI all-sky survey Point Source Catalog (AKARI/PSC). With the two IR instruments, the InfraRed Camera (IRC; Onaka et al. 2007) and the Far-Infrared Surveyor (FIS; Kawada et al. 2007),

Table 1. X-ray and IR properties of the active galactic nuclei, detected both with MAXI and AKARI*.

(1) 2MAXI	(2) Object Name	(3) $F_{\rm S}$	(4) $F_{\rm H}$	(5) HR	(6) f_9	(7) f_{18}	(8) f_{90}	(9) z	(10) type
J0044−238	NGC 235A	0.6 ± 0.3	7.8 ± 1.1	0.64 ± 0.18	—	295 ± 32	—	0.0222	Sy1
J0048+320	Mrk 348	2.8 ± 0.4	21.4 ± 1.3	0.42 ± 0.06	—	593 ± 43	736 ± 60	0.015	Sy2
J0124−349	NGC 526A	5.4 ± 0.4	22.5 ± 1.2	0.16 ± 0.04	141 ± 14	292 ± 26	—	0.0191	Sy1.5
J0124−588	Fairall 0009	4.3 ± 0.3	17.9 ± 1	0.15 ± 0.04	229 ± 20	440 ± 24	—	0.047	Sy1
J0228+314	NGC 931	4.3 ± 0.4	18 ± 1.5	0.15 ± 0.06	349 ± 12	763 ± 48	2430 ± 64	0.0167	Sy1.5
J0233+324	NGC 973	3.9 ± 0.4	16.6 ± 1.5	0.17 ± 0.07	—	93 ± 77	1704 ± 69	0.0162	Sy2
J0334−360	NGC 1365	3.6 ± 0.4	12.9 ± 1.2	0.07 ± 0.07	2234 ± 38	5364 ± 42	80384 ± 13546	0.0055	Sy1.8
J0342−214	ESO 548−G081	3.8 ± 0.3	14.6 ± 1.1	0.11 ± 0.06	—	—	968 ± 61	0.0145	Sy1
J0424−571	1H 0419−577	2.6 ± 0.3	13.4 ± 1.1	0.25 ± 0.06	—	106 ± 21	—	0.104	Sy1.5
J0433+054	3C 120	8.1 ± 0.4	25.4 ± 1.3	0.01 ± 0.04	203 ± 20	497 ± 68	1468 ± 85	0.033	Sy1
J0437−106	MCG −02-12-050	3.2 ± 0.3	12.5 ± 1.2	0.12 ± 0.07	—	—	682 ± 111	0.0364	Sy1.2
J0443+288	UGC 03142	1.7 ± 0.4	11.8 ± 1.2	0.38 ± 0.1	—	—	1581 ± 79	0.0217	Sy1
J0453−752	ESO 033-G 002	4.1 ± 0.3	13.4 ± 0.7	0.03 ± 0.04	163 ± 7	387 ± 15	646 ± 120	0.0181	Sy2
J0516−001	Ark120	6.3 ± 0.4	20.8 ± 1.1	0.04 ± 0.04	252 ± 18	253 ± 33	—	0.0323	Sy1
J0516−102	MCG-02-14-009	2.2 ± 0.3	8.7 ± 1	0.13 ± 0.09	90 ± 21	—	528 ± 56	0.0285	Sy1
J0518−325	ESO 362-18	2.7 ± 0.4	9.4 ± 1.1	0.07 ± 0.09	166 ± 31	366 ± 36	1277 ± 88	0.0125	Sy1.5
J0523−363	PKS 0521−36	3.5 ± 0.4	12.7 ± 1.2	0.08 ± 0.07	96.6 ± 0.1	216 ± 20	—	0.0553	BL Lac
J0552−073	NGC 2110	13.3 ± 0.4	71.1 ± 1.3	0.27 ± 0.02	300 ± 19	566 ± 30	4594 ± 47	0.0078	Sy2
J0554+464	MCG +08-11-011	9.2 ± 0.4	33.7 ± 1.3	0.09 ± 0.03	340 ± 18	1283 ± 35	2377 ± 62	0.0205	Sy1.5
J0615+712	Mrk 3	0.4 ± 0.3	7.2 ± 0.9	0.69 ± 0.17	322 ± 5	1892 ± 49	2939 ± 282	0.0135	Sy2
J0640−257	ESO 490-IG026	2.6 ± 0.3	7.8 ± 1	-0.01 ± 0.09	—	—	1409 ± 41	0.0248	Sy1.2
J0740+497	Mrk 79	2.8 ± 0.4	8.9 ± 1.2	0.03 ± 0.1	276 ± 6	611 ± 38	1358 ± 64	0.0222	Sy1.2
J0804+052	Mrk 1210	0.9 ± 0.4	9.7 ± 1.2	0.55 ± 0.14	274 ± 19	1310 ± 6	1196 ± 61	0.0135	Sy2
J0808+757	PG 0804+761	3 ± 0.3	8.5 ± 0.9	-0.03 ± 0.07	118 ± 10	186 ± 15	—	0.1	Sy1
J0920−079	MCG −01-24-012	3.6 ± 0.4	17 ± 1.2	0.21 ± 0.06	—	263 ± 44	—	0.0196	Sy2
J0923+228	MCG +04-22-042	2.3 ± 0.4	10.3 ± 1.1	0.2 ± 0.09	78 ± 15	178 ± 47	—	0.0323	Sy1.2
J0945−140	NGC 2992	1.3 ± 0.3	9.2 ± 1	0.39 ± 0.11	299 ± 49	826 ± 54	9220 ± 194	0.0077	Sy2
J0947−308	MCG −05-23-016	18.9 ± 0.4	82.9 ± 1.3	0.18 ± 0.01	384 ± 14	1391 ± 21	1277 ± 84	0.0085	Sy2
J1000−313	2MASX J09594263−3112581	3.1 ± 0.4	14.3 ± 1.1	0.19 ± 0.07	85 ± 1	234 ± 5	—	0.037	Sy1
J1023+199	NGC 3227	5.8 ± 0.4	23.2 ± 1.2	0.14 ± 0.04	444 ± 71	1128 ± 44	10596 ± 535	0.0039	Sy1.5
J1031−143	2MASSi J1031543−141651	2.4 ± 0.3	11.7 ± 1.1	0.22 ± 0.08	94 ± 1	—	—	0.086	Sy1
J1105+724	NGC 3516	4.1 ± 0.3	24.8 ± 1	0.33 ± 0.04	262 ± 20	651 ± 16	1317 ± 83	0.0088	Sy1.5
J1139−376	NGC 3783	8.4 ± 0.4	39.7 ± 1.3	0.21 ± 0.03	502 ± 10	1530 ± 41	2716 ± 108	0.0097	Sy1
J1203+445	NGC 4051	5.2 ± 0.4	18.8 ± 1.2	0.08 ± 0.05	346 ± 30	885 ± 42	4557 ± 254	0.0023	Sy1.5
J1210+394	NGC 4151	15.1 ± 0.5	122.6 ± 1.3	0.45 ± 0.01	1032 ± 19	3629 ± 72	4594 ± 126	0.0033	Sy1.5
J1217+073	NGC 4235	2.3 ± 0.4	11.3 ± 1.2	0.24 ± 0.09	—	—	401 ± 50	0.008	Sy1
J1325−429	Centaurus A	34.1 ± 0.5	300.2 ± 1.8	0.48 ± 0.01	10191 ± 2305	13148 ± 1049	102187 ± 12824	0.0018	Sy2
J1335−341	MCG −06-30-015	8.7 ± 0.4	36.2 ± 1.2	0.15 ± 0.03	280 ± 32	591 ± 11	1035 ± 119	0.0077	Sy1.2
J1338+046	NGC 5252	3.5 ± 0.4	22.4 ± 1.2	0.36 ± 0.05	—	—	416 ± 120	0.023	Sy1.9
J1349−302	IC 4329A	18.7 ± 0.4	75.7 ± 1.2	0.14 ± 0.01	769 ± 12	1790 ± 34	1785 ± 210	0.016	Sy1.2
J1413−030	NGC 5506	12.5 ± 0.4	60.3 ± 1.2	0.22 ± 0.02	823 ± 27	2240 ± 69	8413 ± 302	0.0062	Sy1.9
J1417+253	NGC 5548	8.1 ± 0.4	28.8 ± 1.5	0.08 ± 0.03	157 ± 5	409 ± 40	1073 ± 237	0.0172	Sy1.5
J1419−265	ESO 511-G030	1.9 ± 0.3	10.1 ± 1.1	0.28 ± 0.1	—	—	847 ± 150	0.0224	Sy1
J1423+250	NGC 5610	2.1 ± 0.4	11.2 ± 1.5	0.27 ± 0.1	167 ± 19	371 ± 41	5795 ± 205	0.0169	Sy2
J1437+588	Mrk 817	2.7 ± 0.3	9.6 ± 1	0.07 ± 0.08	188 ± 10	669 ± 27	1575 ± 60	0.0314	Sy1.5
J1512−213	2MASX J15115979−2119015	2.5 ± 0.3	10.3 ± 1.1	0.14 ± 0.08	95 ± 8	—	1591 ± 89	0.0446	Sy1
J1513+423	NGC 5899	2 ± 0.4	8.9 ± 1.2	0.19 ± 0.12	—	—	4683 ± 184	0.0086	Sy2
J1535+581	Mrk 290	2.3 ± 0.3	8 ± 1	0.06 ± 0.09	—	151 ± 13	—	0.0296	Sy1
J1548−136	NGC 5995	2.6 ± 0.3	13.9 ± 1	0.27 ± 0.07	325 ± 19	671 ± 4	4580 ± 329	0.0252	Sy2
J1555−793	PKS 1549−79	2.1 ± 0.3	7 ± 0.8	0.04 ± 0.08	82 ± 4	328 ± 45	925 ± 95	0.1501	Sy1
J1614+660	Mrk 876	2.4 ± 0.3	7.5 ± 0.8	0.01 ± 0.08	82 ± 5	178 ± 19	541 ± 39	0.129	Sy1
J1717−628	NGC 6300	0.4 ± 0.3	14.2 ± 1	0.85 ± 0.1	277 ± 24	1336 ± 97	14928 ± 1066	0.0037	Sy2
J1834+327	3C 382	7.3 ± 0.4	29.1 ± 1.3	0.13 ± 0.04	120 ± 12	—	—	0.0579	Sy1
J1836−594	Fairall 0049	4 ± 0.3	14.8 ± 0.9	0.09 ± 0.05	411 ± 20	920 ± 59	2619 ± 180	0.0202	Sy2
J1838−654	ESO 103-035	2.5 ± 0.3	25.4 ± 0.9	0.55 ± 0.04	300 ± 25	1446 ± 12	1227 ± 77	0.0133	Sy2
J1842+797	3C 390.3	7.7 ± 0.3	30.8 ± 0.9	0.13 ± 0.03	90 ± 10	242 ± 17	—	0.0561	Sy1
J1845−626	Fairall 0051	1.5 ± 0.3	7.1 ± 0.8	0.21 ± 0.11	301 ± 7	697 ± 62	1705 ± 180	0.0142	Sy1
J1921−587	ESO 141-G055	8 ± 0.3	26.2 ± 1	0.04 ± 0.03	150 ± 5	233 ± 38	—	0.036	Sy1
J1937−060	2MASX J19373299−0613046	5.8 ± 0.4	19.1 ± 1.1	0.04 ± 0.04	—	718 ± 28	3709 ± 127	0.0103	Sy1.5
J2009−611	NGC 6860	3.4 ± 0.3	12.1 ± 0.9	0.08 ± 0.06	155 ± 13	357 ± 61	1369 ± 73	0.0149	Sy1
J2042+751	4C +74.26	5.2 ± 0.3	21.4 ± 0.9	0.15 ± 0.04	147 ± 6	175 ± 9	—	0.104	Sy1
J2044−106	Mrk 509	11.6 ± 0.4	42.5 ± 1.2	0.09 ± 0.02	247 ± 18	499 ± 17	—	0.0344	Sy1.2
J2115+821	2MASX J21140128+8204483	2.7 ± 0.3	9.6 ± 0.9	0.07 ± 0.07	71 ± 5	105 ± 32	—	0.084	Sy1
J2136−624	1RXS J213623.1−622400	4.1 ± 0.3	18.4 ± 0.9	0.2 ± 0.04	—	142 ± 11	—	0.0588	Sy1
J2200+105	Mrk 520	1.3 ± 0.4	9.6 ± 1.2	0.41 ± 0.12	146 ± 12	320 ± 11	5040 ± 100	0.0266	Sy1.9
J2201−317	NGC 7172	2.2 ± 0.4	25.2 ± 1.2	0.57 ± 0.05	316 ± 17	424 ± 44	8087 ± 218	0.0087	Sy2
J2238−126	Mrk 915	2 ± 0.3	8.4 ± 1	0.17 ± 0.1	—	482 ± 284	—	0.0241	Sy1
J2303+086	NGC 7469	6.6 ± 0.4	21.7 ± 1.2	0.03 ± 0.04	767 ± 17	2692 ± 60	27694 ± 1738	0.0163	Sy1.2
J2304−085	Mrk 926	10.5 ± 0.4	38 ± 1.2	0.09 ± 0.02	60 ± 3	214 ± 36	647 ± 119	0.0469	Sy1.5
J2318+001	NGC 7603	3.6 ± 0.4	13.4 ± 1.2	0.1 ± 0.07	295 ± 11	321 ± 12	1340 ± 104	0.0295	Sy1.5

* Remarks:
(1) Source name in the 2MAXI catalog.
(2) Name of the optical counterpart.
(3), (4) Soft (3 – 4 keV) and hard (4 – 10 keV) band X-ray flux in the unit of 10^{-12} ergs cm^{-2} s^{-1} (Hiroi et al. 2013)
(5) X-ray Hardness ratio, defined as $HR = (F'_{\rm H} - F'_{\rm S})/(F'_{\rm H} + F'_{\rm S})$, where $F'_{\rm H}$ and $F'_{\rm S}$ is the hard and soft band fluxes in the Crab unit;
i.e., $F'_{\rm H} = F_{\rm H}/1.21 \times 10^{-8}$ ergs cm^{-2} s^{-1} and $F'_{\rm S} = F_{\rm S}/3.98 \times 10^{-9}$ ergs cm^{-2} s^{-1} (see Hiroi et al. 2013)
(6) – (8) IR flux density at 9 μm, 18 μm and 90 μm in mJy of the AKARI counterpart (Ishihara et al. 2010; Yamamura et al. 2012)
(9) Object redshift.
(10) Optical Seyfert type (Hiroi et al. 2013; and reference therein).

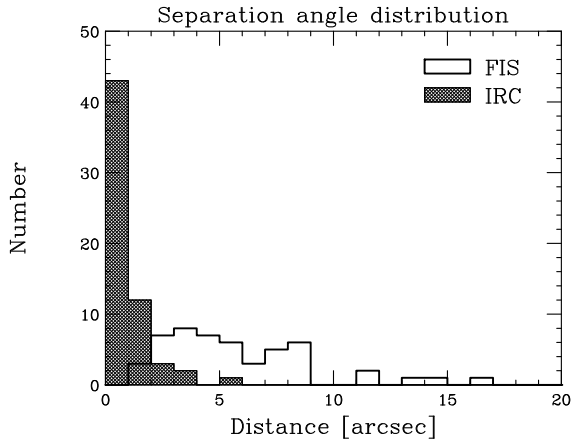

Fig. 1. Distribution of the separation angle between the optical position of the Seyfert galaxies in the 2MAXI catalog and their AKARI counterparts. The hatched and thick histograms indicate the distributions of the IRC and FIS counterparts, respectively.

the AKARI/PSC widely covers the mid-to-far IR sources in the 9–160 μm range, where the dust torus is expected to radiate a significant fraction of its energy. Therefore, a combined use of the 2MAXI catalog and AKARI/PSC helps us to investigate the vicinity of the active galactic nuclei, and to reveal the nature of the dust torus.

2 Sample

2.1 The second MAXI all-sky X-ray source catalog

The 2MAXI catalog (Hiroi et al. 2013)[1] was constructed from all-sky X-ray survey data accumulated with the gas slit camera (Mihara et al. 2011; Sugizaki et al. 2011) onboard MAXI in the first 37 months from 2009 September to 2012 October. The catalog lists 500 X-ray sources detected at high Galactic latitude of $|b| \geq 10^\circ$ with a significance of $> 7\sigma$ in the $4-10$ keV range. Its 7σ detection sensitivity, 7.5×10^{-12} erg cm^{-2} s^{-1} in $4-10$ keV for about half of the sky, is highest among those of previous all-sky X-ray surveys in the similar energy range. The X-ray flux of the faintest source in the catalog is measured as 4.7×10^{-12} erg cm^{-2} s^{-1}.

Hiroi et al. (2013) cross-matched all the 2MAXI X-ray sources to previous X-ray source catalogs, including the first MAXI catalog (Hiroi et al. 2011), the meta-catalog of X-ray detected clusters of galaxies (Piffaretti et al. 2011), and the Swift/BAT 70-month catalog (Baumgartner et al. 2013). As a result, they reported that 292 2MAXI sources have a probable single counterpart. In the following, we assume that these are real counterparts to the 2MAXI sources. In addition, multiple candidate counterparts were eventually found for 4 sources, mostly due to the moderate position uncertainty of the 2MAXI catalog (90% error radius of $\sim 0.5^\circ$ for 7σ sources; Hiroi et al. 2013). Thus, the current completeness of source identification to the 2MAXI catalog is about ~ 58%. For the remaining 204 sources, identification studies are ongoing (private communication with the MAXI team).

Table 2. Statistics of Source Identification

Type	Sy1	Sy2	Sy1+Sy2
$N_{\rm X}{}^*$	68	27	95
$N_{IR}{}^\dagger$	48	21	69
$N_9{}^\ddagger$	36	16	52
$N_{18}{}^\ddagger$	38	19	57
$N_{90}{}^\ddagger$	30	20	50

* Number of the Seyfert galaxies listed in the 2MAXI catalog.
† Number of the 2MAXI Seyfert galaxies, that have an AKARI counterpart in at least one of the three photometric bands.
‡ Number of the 2MAXI Seyfert galaxies, detected at 9 μm (N_9), 18 μm (N_{18}) or 90 μm (N_{90}).

In the present study, all the active galactic nuclei tabulated in the 2MAXI catalog were picked up; these consist of 95 Seyfert galaxies, 5 quasars, and 15 blazars including BL Lacertae objects. We noticed that all of these sources are listed in the Swift/BAT 70-month catalog. We refer to the 2MAXI catalog (and references therein) for their source name, the 3-year averaged X-ray fluxes in the 3–4 keV and 4–10 keV ranges ($F_{\rm S}$ and $F_{\rm H}$, respectively), X-ray hardness ratio between these bands HR (its definition is discussed in §3.2), optical position, redshift z, and object type (optical classification).

2.2 The AKARI point source catalog

The AKARI/PSC is electrically available at the AKARI Catalogue Archive Server (Yamauchi et al. 2011) [2]. The catalog contains $870,973$ mid-IR sources (Ishihara et al. 2010) and $427,071$ far-IR ones (Yamamura et al. 2012), detected with the IRC and the FIS, respectively. The IRC is equipped with 2 photometric bands at the effective wavelength of $\lambda = 9$ μm and 18 μm. The IRC sensitivity for an 80% detection completeness is 0.12 Jy and 0.22 Jy at 9 μm and 18 μm, respectively. The FIS has 4 photometric bands centered at $\lambda = 65$ μm, 90 μm, 140 μm, and 160 μm. In the present study, we refer only to 90 μm FIS sources, since the sensitivity at this band (the 80% completeness limit of 0.43 Jy) is nearly an order of magnitude better than those at the other 3 bands. The typical position accuracy of the IRC and FIS sources is $\sim 3''$ and $\sim 6''$, respectively.

A quality flag, indicating a reliability of the source detection and flux determination, is assigned to each AKARI source

[1] Electrically available at http://vizier.cfa.harvard.edu/viz-bin/VizieR?-source=J/ApJS/207/36 [2] http://darts.isas.jaxa.jp/astro/akari/cas.html

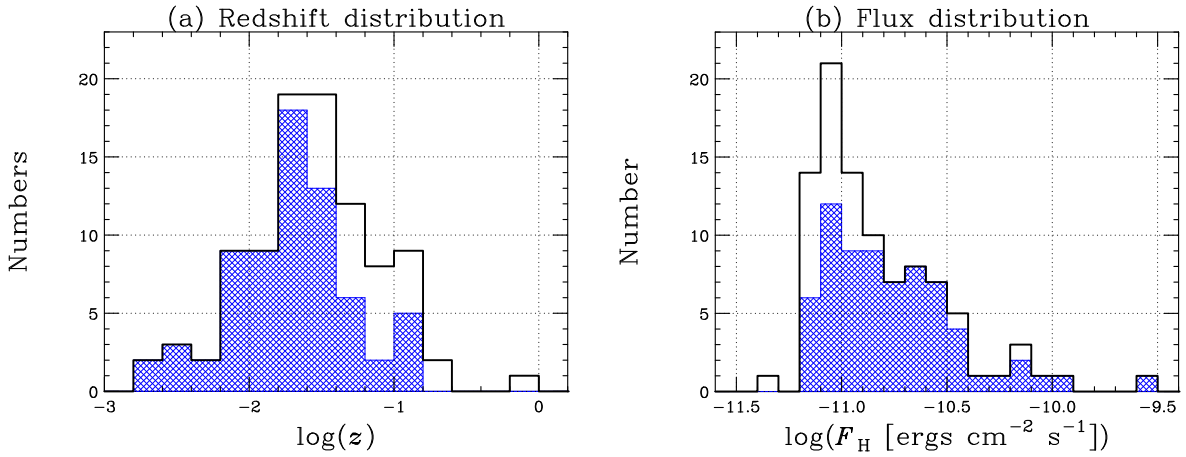

Fig. 2. Distributions of the redshift z (panel a) and 4–10 keV X-ray flux $F_{\rm H}$ (panel b). The thick histograms indicate the distributions for all the Seyfert galaxies in the 2MAXI catalog, while the hatched histograms show the distributions for those with an AKARI counterpart.

for the individual photometric bands. According to the recommendation from the AKARI team, we adopted only the AKARI sources with a quality flag of 3, which assures a high flux accuracy. The same criterion was commonly adopted in similar studies (e.g., Matsuta et al. 2012; Ichikawa et al. 2012; Terashima et al. 2015).

2.3 Source identification

We searched the AKARI/PSC for IR counterparts to the active galaxies selected from the 2MAXI catalog. For the source identification, we referred to the optical position of the individual 2MAXI sources, instead of their position determined with MAXI. A search radius of $10''$ and $20''$ was adopted for the IRC and FIS catalog, respectively, since these values nearly correspond to their 3σ position accuracy. The same angular threshold was widely imposed in previous studies (e.g., Matsuta et al. 2012).

The result of the source identification is summarized in table 1, where the X-ray properties ($F_{\rm H}$, $F_{\rm S}$, and HR) and IR flux densities at 9 μm, 18 μm, and 90 μm (f_9, f_{18}, and f_{90} respectively) are tabulated for those listed in both the 2MAXI catalog and AKARI/PSC, together with their optical information. Figure 1 plots the distribution of the angular separation between the 2MAXI sources and their AKARI counterparts. As shown with the hatched histogram, the IRC counterparts are concentrated at a relatively narrow range with a separation of $\lesssim 6'$. Due to the slightly worse angular resolution at the longer wavelength, the distribution of the FIS sources (up to $\sim 17'$ as indicated by the thick histogram) is wider than that of the IRC sources. These trends are qualitatively consistent with the previous study by Ichikawa et al. (2012).

No AKARI counterpart was found to the 5 quasars in the 2MAXI catalog. This is reasonable because these quasars are a relatively high-redshift and faint source ($z > 0.17$ and $F_{\rm H} < 1.5 \times 10^{-11}$ erg cm^{-2} s^{-1}; see figure 2). Among 15 blazars, only one BL Lacertae object PKS 0521−36, corresponding to the MAXI X-ray source 2MAXI J0523−363 with a hard and soft X-ray flux of $F_{\rm H} = (12.7 \pm 1.2) \times 10^{-12}$ erg cm^{-2} s^{-1}and $F_{\rm S} = (3.5 \pm 0.4) \times 10^{-12}$ erg cm^{-2} s^{-1} respectively, was identified with an AKARI source with 9 μm and 18 μm IR flux densities of $f_9 = 96.6 \pm 0.1$ mJy and $f_{18} = 216 \pm 20$ mJy, respectively. Therefore, in the statistical argument below, we deal only with Seyfert galaxies.

Statistics of the source matching for the Seyfert galaxies between the 2MAXI catalog and AKARI/PSC are summarized in Table 2. Among the 95 2MAXI Seyfert galaxies, 69 ones ($\sim 73\%$) were successfully identified with an AKARI source at least at one of the three photometric bands. The number of the 2MAXI Seyfert galaxies detected at 9 μm, 18 μm, and 90 μm is $N_9 = 52$, $N_{18} = 57$, and $N_{90} = 50$, respectively. Out of the 68 type-1 Seyfert (Sy1) galaxies, including those optically categorized into Sy1.2 and Sy1.5 sources, 48 ($\sim 71\%$) are found to have an AKARI counterpart ($N_9 = 36$, $N_{18} = 38$, and $N_{90} = 30$), while 21 out of 27 type-2 Seyfert (Sy2) galaxies ($\sim 78\%$), including Sy1.8 and Sy1.9 objects, were detected with AKARI ($N_9 = 16$, $N_{18} = 19$, and $N_{90} = 20$).

The redshift distribution of the 2MAXI Seyfert galaxies is displayed in the panel (a) of figure 2. Their average redshift was evaluated as $\overline{z} \simeq 0.048$. When we focus on the objects with an AKARI counterpart, the average redshift reduces to $\overline{z} \simeq 0.03$. All the 2MAXI Seyfert galaxies located at $z < 0.023$ (41 ones) are detected with AKARI. In contrast, only 5 Seyfert galaxies (out of 12 ones) at $z > 0.1$ are found to have an AKARI counterpart, with PKS 1549−79 (Sy1) being the most distant one ($z = 0.1501$). Thus, our final sample is limited to local sources mainly at $z \lesssim 0.1$.

The 4–10 X-ray flux, $F_{\rm H}$, of the 2MAXI Seyfert galaxies

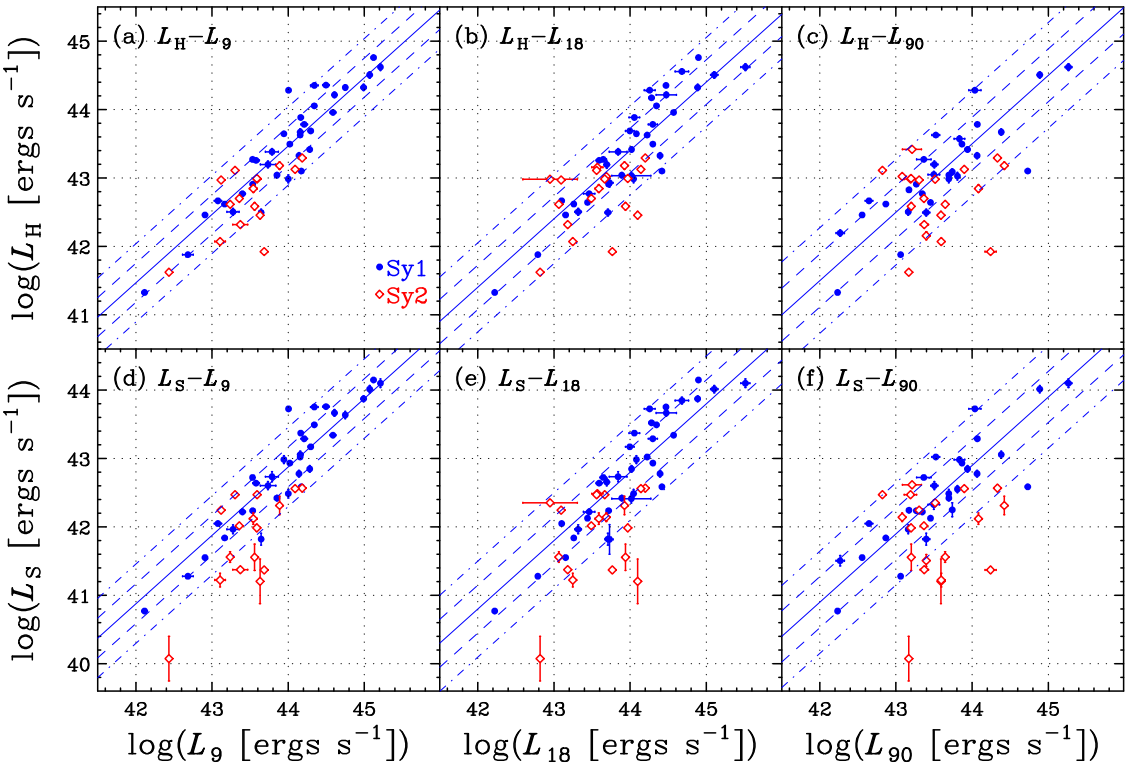

Fig. 3. Relation between the observed X-ray and IR luminosities; (a) $L_{\rm H}-L_9$, (b) $L_{\rm H}-L_{18}$, (c) $L_{\rm H}-L_{90}$, (d) $L_{\rm S}-L_9$, (e) $L_{\rm S}-L_{18}$, and (f) $L_{\rm S}-L_{90}$. The Sy1 and Sy2 galaxies are plotted with the filled blue circles and open red diamonds, respectively. The logarithmic average of the X-ray to IR luminosity ratio for the Sy1 galaxies is shown with the solid line in each panel, while the $1\sigma_{\rm r}$ and $2\sigma_{\rm r}$ ranges are indicated by the dashed and dash-dotted lines, respectively.

is distributed as shown in the panel (b) of figure 2. The X-ray brightest source in the sample is Centaurus A, with an X-ray flux of $F_{\rm H}=3.00\times10^{-10}$ erg cm^{-2} s^{-1} averaged over the 3 years. It is reasonable that the objects, that are not detected with AKARI, are mainly the fainter ones with an X-ray flux of $F_{\rm H}\lesssim 1\times10^{-11}$ erg cm^{-2} s^{-1}. Above this flux threshold, 59 out of 67 objects ($\sim$86%) were found to coincide with an AKARI source. Among the objects without any AKARI counterpart, the X-ray brightest one is the Sy1.9 galaxy 2MASX J09235371−3141305 with a hard-band X-ray flux of $F_{\rm H}=6.35\times10^{-11}$ erg cm^{-2} s^{-1}.

3 Results

3.1 Relation between the X-ray and IR luminosities

In figure 3, the soft- and hard-band X-ray luminosities, $L_{\rm S}$ and $L_{\rm H}$ respectively, of the 69 Seyfert galaxies tabulated in both the 2MAXI and AKARI catalogs, are plotted against their IR ones at 9 μm, 18 μm and 90 μm, L_9, L_{18} and L_{90}. The solid line on each panel corresponds to the average of the X-ray-to-IR luminosity ratio among the Sy1 galaxies evaluated in the logarithmic space, while the dashed and dash-dotted lines show its $1\sigma_{\rm r}$ and $2\sigma_{\rm r}$ ranges, respectively, where $\sigma_{\rm r}$ indicates the standard deviation of the logarithmic luminosity ratio. Here, the X-ray flux observed with MAXI was simply converted into the luminosity as $L_i=4\pi D_{\rm L}^2F_i$ ($i=$ H and S for the hard and soft band respectively). The source redshift z was transformed to the luminosity distance $D_{\rm L}$, by assuming the cosmological constants of $H_0=71$ km s^{-1} Mpc^{-1}, $\Omega_{\rm M}=0.27$, and $\Omega_\Lambda=0.73$. The monochromatic IR luminosity was calculated from the flux density at each photometric band as $L_\lambda=4\pi D_{\rm L}^2\nu_\lambda f_\lambda$, where ν_λ is the representative frequency of the AKARI photometric bands (i.e., $\lambda=9$ μm, 18 μm, and 90 μm). We neglected the so-called K-correction because the sample is limited to the low-redshift sources, as shown in figure 2. Even for the most distant source in the sample, PKS 1549−79 located at $z=0.1501$, the effect of the K-correction on its luminosity is evaluated as less than a few %.

Figure 3 suggests that the X-ray luminosities of the Sy1 galaxies in the 2MAXI-AKARI sample linearly correlates with the IR ones in the logarithmic space, while the correlation appears to be rather vague for the Sy2 sources. In order to quantify such a correlation, we calculated the Spearman's rank correlation coefficient ($\rho_{\rm L}$), between the X-ray and IR luminosities in the logarithmic space. This coefficient was commonly adopted for similar studies (e.g., Matsuta et al. 2012; Ichikawa et al. 2012). The result is summarized in table 3. A tight correlation was confirmed for the Sy1 galaxies with $\rho_{\rm L}\sim0.9$. In contrast,

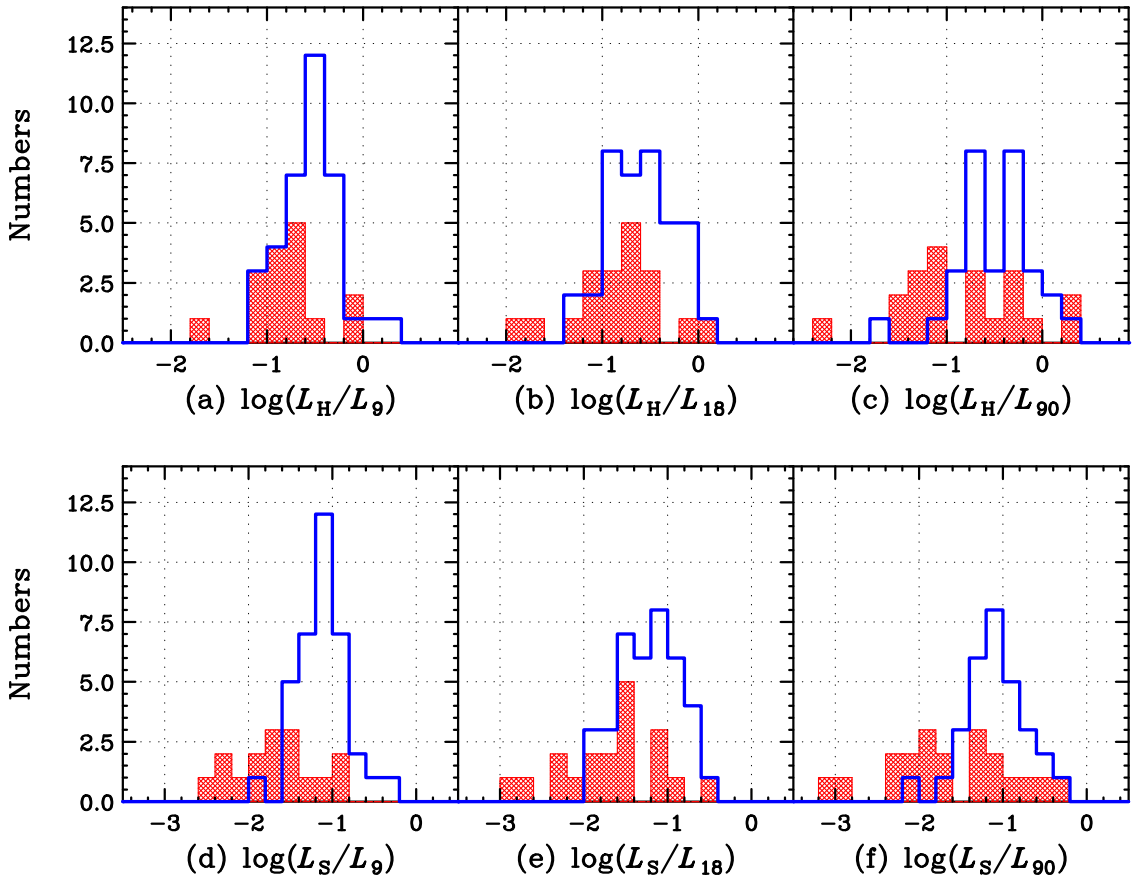

Fig. 4. Distributions of the absorption-inclusive X-ray to IR luminosity ratio in the logarithmic space; (a) $\log(L_{\rm H}/L_9)$, (b) $\log(L_{\rm H}/L_{18})$, (c) $\log(L_{\rm H}/L_{90})$, (d) $\log(L_{\rm S}/L_9)$, (e) $\log(L_{\rm S}/L_{18})$, and (f) $\log(L_{\rm S}/L_{90})$. The distributions of the Sy1 and Sy2 galaxies are indicated with the thick blue and hatched red histograms respectively.

the X-ray luminosities of the Sy2 objects are found to exhibit a moderate correlation to the mid-IR luminosities ($\rho_{\rm L} \simeq 0.3$–0.5 to $\log(L_9)$ and $\log(L_{18})$), and no meaningful one to the far-IR luminosity ($\rho_{\rm L} \sim 0$ to $\log(L_{90})$). After the Sy2 galaxies are added to the Sy1 ones (indicated as Sy1+Sy2 in table 3), the coefficients to $\log(L_9)$ and $\log(L_{18})$ still indicate a strong correlation ($\rho_{\rm L} \gtrsim 0.8$), while those to $\log(L_9)$ decreased to a moderate value ($\rho_{\rm L} \sim 0.6$).

We also evaluated the Spearman's rank correlation coefficients between the logarithms of the observed X-ray fluxes and IR flux densities ($\rho_{\rm F}$), and tabulate them in table 4. In the case of flux-limited samples, the flux correlation is useful, since it is free from artifacts due to the source redshift. A comparison between the results in tables 3 and 4 pointed out that $\rho_{\rm F}$ exhibits a similar trend to $\rho_{\rm L}$, except for the fact that the tight luminosity correlation suggested for the Sy1 and Sy1+Sy2 categories has reduced to a moderate one in the flux space ($\rho_{\rm F} = 0.4$–0.6). We think that this is probably because the observed X-ray flux range (typically $\log(F_{\rm H}) = -11.0$–-10.5 as shown in figure 2) is only comparable to the dispersion of the X-ray-to-IR flux/luminosity ratio (see below).

Figure 4 plots the distribution of the X-ray-to-IR luminosity ratio for the 2MAXI-AKARI sample in the logarithmic space. The Sy1 galaxies are found to be distributed in a relatively narrow range with $\sigma_{\rm r} \simeq 0.3$–$0.4$ (corresponding to a factor of 2–3 in the linear space). This range is found to be similar to those reported in the previous studies (e.g., Matsuta et al. 2012; Ichikawa et al. 2012). In contrast, the observed X-ray luminosity of the Sy2 galaxies tends to be lower than that of the Sy1 galaxies with a similar IR luminosity. This is clearly visualized in figure 3 where the majority of the Sy2 galaxies are located below the solid line, indicating the logarithmic average of the X-ray-to-IR luminosity ratio for the Sy1 galaxies. This trend is more prominent in the soft X-ray band, as is clearly indicated in figure 4. As we discuss in §4.1, this tendency is basically attributable to X-ray absorption.

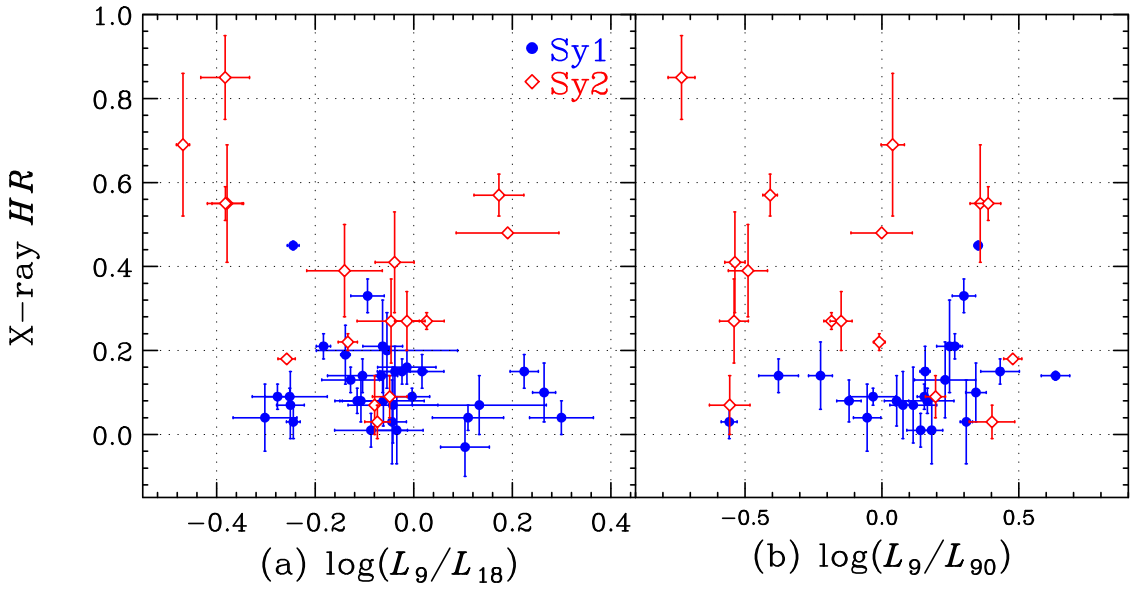

Fig. 5. The relation between the X-ray hardness HR and IR colors. In panels (a) and (b), HR is plotted against $\log(L_9/L_{18})$ and $\log(L_9/L_{90})$, respectively. The filled blue circles indicate the Sy1 galaxies, while the open red diamonds point the Sy2 galaxies.

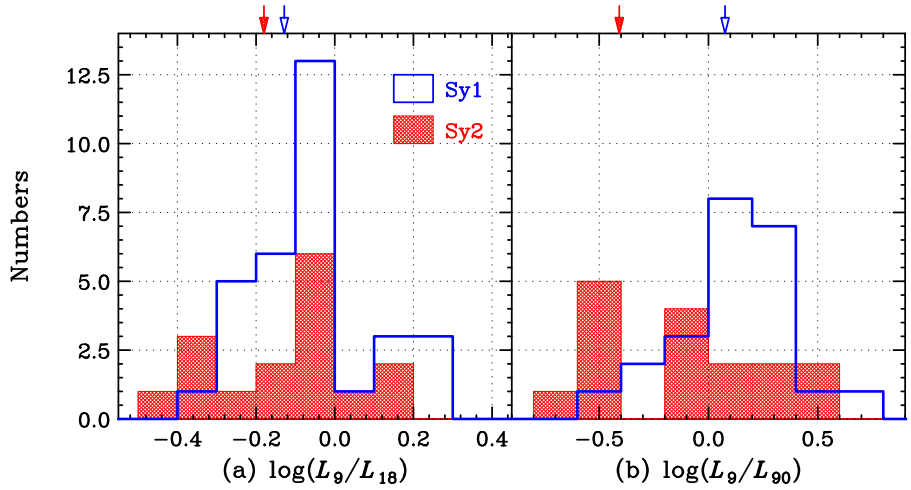

Fig. 6. Distributions of the IR colors among the 2MAXI-AKARI Seyfert galaxies. The panels (a) and (b) display the distributions of $\log(L_9/L_{18})$ and $\log(L_9/L_{90})$, respectively. The thick blue and hatched red histograms indicate the distributions of the Sy1 and Sy2 galaxies, respectively. The open blue and filled red arrows on the top of the figure represent the mean IR color of the Sy1 and Sy2 galaxies, respectively, in the 9-month Swift/BAT sample, estimated from Ichikawa et al. (2012).

3.2 Color-color plot

In figure 5, the X-ray hardness ratio HR, representing the X-ray spectral color, is plotted against the IR colors L_9/L_{18} and L_{18}/L_{90} for the 2MAXI-AKARI Seyfert sample. The X-ray hardness, taken from Hiroi et al. (2013), is defined as $HR = (F'_{\rm H} - F'_{\rm S})/(F'_{\rm H} + F'_{\rm S})$, where $F'_{\rm H} = F_{\rm H}/F_{\rm H,C}$ and $F'_{\rm S} = F_{\rm S}/F_{\rm S,C}$ represent the X-ray fluxes normalized to the Crab ones in the hard and soft bands, respectively ($F_{\rm H,C} = 1.21 \times 10^{-8}$ erg cm^{-2} s^{-1} and $F_{\rm S,C} = 3.98 \times 10^{-9}$ erg cm^{-2} s^{-1}). This means that a Crab-like X-ray spectrum with a photon index of $\Gamma = 2.1$ and $N_{\rm H} = 3.5 \times 10^{21}$ cm^{-2} (Kirsch et al. 2005) corresponds to $HR = 0$.

Figure 5 helps us to discriminate the Sy1 galaxies from the Sy2 ones. On the color-color plots, the Sy1 objects tend to concentrate in a relatively narrow area represented by $0 \lesssim HR \lesssim 0.2$ and $|\log(L_9/L_{18})| \lesssim 0.3$, or $|\log(L_9/L_{90})| \lesssim 0.6$. Compared to the Sy1 sources, the Sy2 ones exhibit a rather hard X-ray spectrum, with a typical X-ray hardness of $HR \gtrsim 0.2$.

We accumulated the IR-color distributions of the sample, as shown in figure 6. The arrows on the top of each panel indicate the IR colors, which were estimated from the average spectral energy distribution of the Sy1 and Sy2 galaxies in the 9-month Swift/BAT sample taken from Ichikawa et al. (2012). Thus, the IR color of the 2MAXI sample is consistent to that of

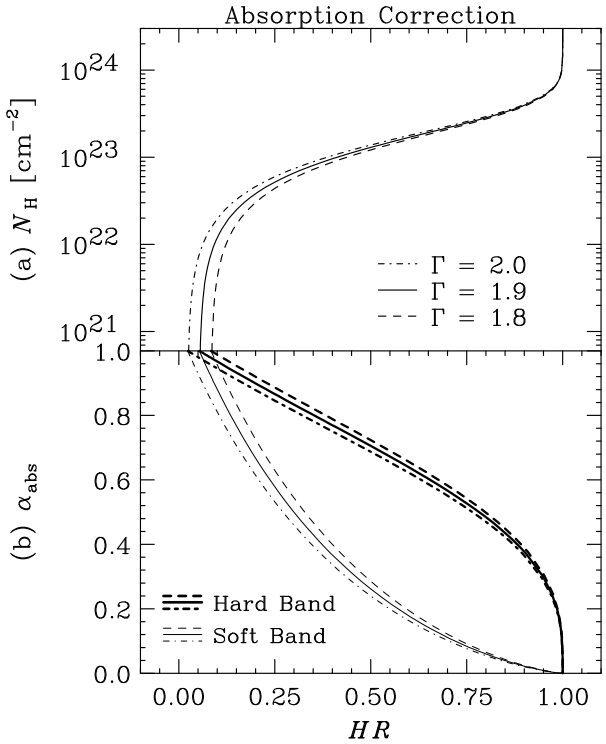

Fig. 7. (a) The line-of-sight hydrogen column density, $N_{\rm H}$, plotted as a function of the X-ray hardness, HR, derived with MAXI. The model predictions, corresponding to the intrinsic photon index of $\Gamma = 1.8, 1.9$, and 2.0, are indicated with the dashed, solid and dash-dotted lines, respectively. (b) The absorbed-to-intrinsic flux ratio $\alpha_{\rm abs}$ in the soft (thin lines) and hard (thick lines) bands, plotted against HR.

the 9-month Swift/BAT sample. We found no significant difference in the mid-IR color, $\log(L_9/L_{18})$, between the two Seyfert classes, although there are a few relatively red Sy2 galaxies with Mrk 3 being the reddest one with $\log(L_9/L_{18}) = -0.47$. In contrast, the distribution of the mid-to-far IR color, $\log(L_{18}/L_{90})$, seems to rather differ between the Sy1 and Sy2 galaxies in the sense that the Sy2 galaxies tend to show a redder mid-to-far IR color with $\log(L_{18}/L_{90}) \lesssim 0$. From the K-S test, the probability of the difference between the two source categories was estimated as $\sim 95\%$

4 Discussion

4.1 Absorption column density estimated from HR

The X-ray continuum from Seyfert galaxies in the 2–10 keV range is thought to be basically dominated by the direct nuclear X-ray emission, which is absorbed by their dust torus, except for Compton-thick sources (e.g., Gilli et al. 2007; Ueda et al. 2014). Because X-ray photons in the soft band are more easily subjected to absorption than those in the hard band, an object with higher absorption column density is predicted to exhibit a harder X-ray spectrum (at least in the Compton-thin regime). Therefore, the higher X-ray hardness observed from the Sy2 objects, which is clearly visualized in figure 5, is naturally ascribed to the X-ray absorption.

From the X-ray hardness ratio derived with MAXI, we can roughly estimate the absorbing column density of the dust torus (Ueda et al. 2011). Here, we simply assume that the dominant X-ray spectral component from the Seyfert nuclei in the MAXI energy range is described with an absorbed power-law model. Panel (a) of figure 7 displays the relation of the line-of-sight hydrogen column density, $N_{\rm H}$, to the MAXI hardness, HR, for some representative values of the photon index ($\Gamma = 1.8, 1.9$, and 2.0). This figure indicates that the HR value is sensitive to the X-ray absorption in the range of $N_{\rm H} = 10^{22}$–5×10^{23} cm^{-2} (i.e., in the Compton-thin regime). In panel (b) of figure 7, the ratio of the absorbed X-ray flux to the intrinsic one, $\alpha_{\rm abs}$, is plotted against HR. It is possible to estimate the absorption-corrected intrinsic flux/luminosity of the objects in our sample, by dividing $\alpha_{\rm abs}$ into their flux/luminosity observed with MAXI.

In order to validate the method for absorption correction, we here focus on Centaurus A, the brightest Seyfert (Sy2) galaxy in the sample. Based on the result presented in figure 7 (a), the hardness ratio of this object measured with MAXI, $HR = 0.48 \pm 0.1$, is converted into the column density of $N_{\rm H} \simeq 1.2 \times 10^{23}$ cm^{-2}. From a close examination on the 0.5 – 300 keV wide-band X-ray spectrum of Centaurus A obtained with Suzaku in 2005, Markowitz et al. (2007) revealed that its dominant power-law component in the 2 – 10 keV range, with a photon index of $\Gamma = 1.8$ – 1.85, is subjected to X-ray absorption with a column density of $N_{\rm H} = 1.5 \times 10^{23}$ cm^{-2}. A similar $N_{\rm H}$ value was recently derived in a coordinated observation with NuStar and XMM-Newton performed in 2013 (Fürst et al. 2016). The hydrogen column density inferred from the X-ray hardness with MAXI agrees with these results. From the panel (b) of figure 7, the systematic uncertainty on $\alpha_{\rm abs}$ (and hence the intrinsic luminosity estimate) due to the difference between the MAXI and Suzaku results on $N_{\rm H}$ is evaluated as at most $\sim 30\%$.

4.2 X-ray-to-IR luminosity relation after the absorption correction

By the method demonstrated in §4.1, we evaluated the absorption-corrected intrinsic X-ray luminosities of the 2MAXI-AKARI Seyfert galaxies as $L_{\rm i,cor} = L_{\rm i}/\alpha_{\rm abs}$ (i = H and S). For the absorption correction, we adopted the typical photon index of the Seyfert galaxies, $\Gamma = 1.9$ (e.g., Ueda et al. 2014). No correction was performed to the sources with the hardness smaller than $HR = 0.06$ (corresponding to $\alpha_{\rm abs} = 0.98$ and 0.99 in the soft and hard bands respectively), since we think that the absorption put only a negligible impact on these sources. The relation between the X-ray and the IR luminosities after the ab-

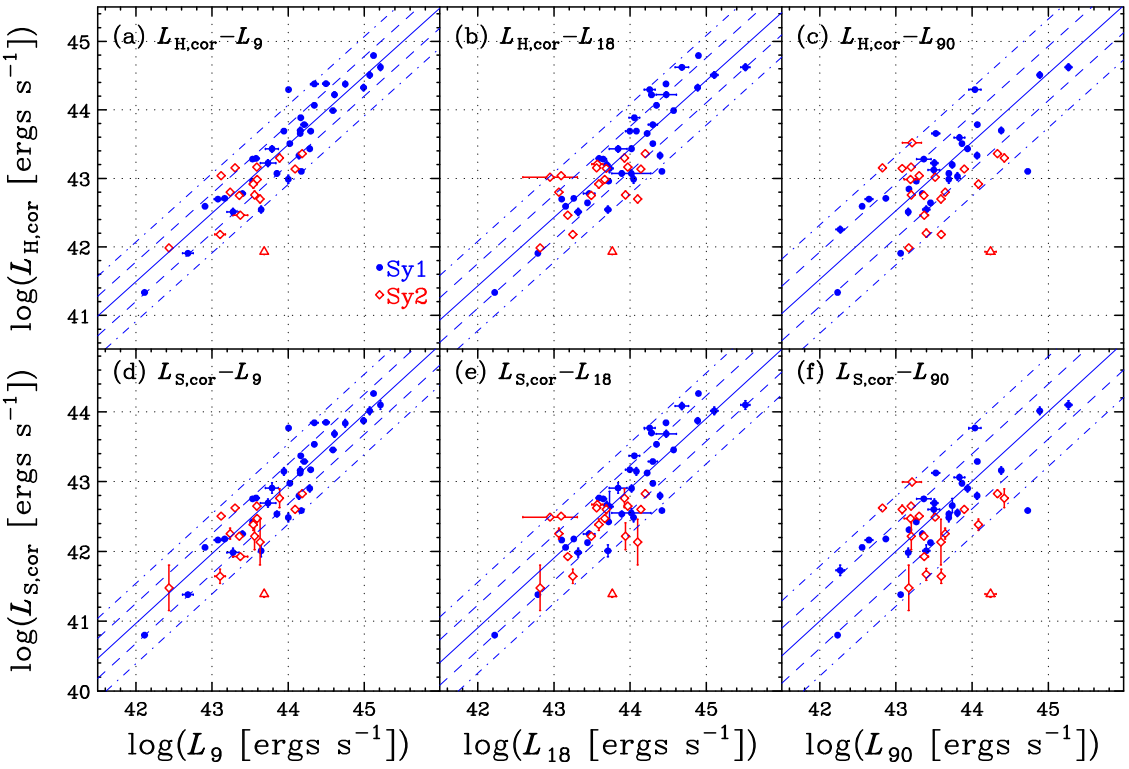

Fig. 8. The absorption-corrected X-ray luminosities plotted against the observed IR luminosities; (a) $L_{\rm H,cor} - L_9$, (b) $L_{\rm H,cor} - L_{18}$, (c) $L_{\rm H,cor} - L_{90}$, (d) $L_{\rm S,cor} - L_9$, (e) $L_{\rm S,cor} - L_{18}$, and (f) $L_{\rm S,cor} - L_{90}$. The same symbol and color notations as for figure 3 are adopted, except for the open triangles indicating NGC 1365.

sorption correction is displayed in figure 8.

After the absorption correction, we re-evaluated the X-ray-to-IR correlation coefficients, $\rho_{\rm L}$ and $\rho_{\rm F}$, and summarize them in tables 3 and 4, respectively. It is found that the correction put only a minor impact on both $\rho_{\rm L}$ and $\rho_{\rm F}$, in comparison to those before the correction. When we take all the Sy1 and Sy2 objects into account, the absorption-removed X-ray luminosities are found to highly correlate to the 9 μm and 18 μm mid-IR luminosities ($\rho_{\rm L} \gtrsim 0.8$), while their correlation to the 90 μm far-IR luminosity is moderate ($\rho_{\rm L} \sim 0.6$). The flux correlation coefficients of the X-ray to mid-IR wavelengths indicate a moderate correlation ($\rho_{\rm F} = 0.4$–0.5), while those to the far-IR band correspond to a weak correlation ($\rho_{\rm F} \sim 0.3$).

Figure 9 shows the histograms of the X-ray-to-IR luminosity ratio in the logarithmic space, after the X-ray absorption was corrected. Thanks to the correction, the Sy2 galaxies have typically moved into the $2\sigma_{\rm r}$ range of the Sy1 galaxies (i.e., the regions between the dash-dotted lines on figure 8). This result is thought to reinforce the X-ray-to-IR luminosity/flux correlation throughout the Sy1 and Sy2 galaxies. For comparison, we estimated the X-ray-to-IR color of the 9-month and 22-month Swift/BAT samples derived in the previous studies by Ichikawa et al. (2012) and Matsuta et al. (2012), respectively. The ratios of the 14–195 keV X-ray luminosity to the IR ones and their errors, both of which are presented in Ichikawa et al. (2012) and Matsuta et al. (2012), were converted to match the MAXI energy range, by assuming a power-law like X-ray spectrum with a photon index of $\Gamma = 1.9$. The horizontal arrows in figure 9 indicate the $1\sigma_{\rm r}$ range of the X-ray-to-IR luminosity ratio, thus obtained, for the 9-month and 22-month Swift/BAT samples. Our result from the 2MAXI sample is found to be consistent to the Swift/BAT results.

A number of recent researches indicate that the intrinsic X-ray luminosity of Seyfert galaxies tightly correlates with their observed IR luminosities, irrespective of their optical classification (e.g., Gandhi et al. 2009; Matsuta et al. 2012; Ichikawa et al. 2012). The correlation is widely interpreted under the framework of the so-called clumpy torus geometry (e.g., Krolik & Begelman 1988), since the simple torus model with a smooth dust distribution infers a significant dust extinction to the IR luminosity for obscured (i.e., type-2) sources.

Figures 8 and 9, together with the correlation coefficients summarized in tables 3 and 4, support the X-ray-to-IR correlation, especially that to the mid-IR band. Basically, these mean that our result strengthens the clumpy torus scenario. Most of the previous results were usually based on the hard X-ray survey above 10 keV (Matsuta et al. 2012; Ichikawa et al. 2012), or a small sample below 10 keV derived in a restricted sky

Table 3. Summary of the Spearman's rank correlation coefficients, $\rho_{\rm L}$, between the X-ray and IR luminosities.

		IR luminosity		
Type	X-ray luminosity	$\log(L_9)$	$\log(L_{18})$	$\log(L_{90})$
Sy1	$\log(L_{\rm H})$	0.92	0.89	0.88
	$\log(L_{\rm H,cor})$	0.91	0.89	0.86
	$\log(L_{\rm S})$	0.92	0.89	0.89
	$\log(L_{\rm S,cor})$	0.92	0.88	0.87
Sy2	$\log(L_{\rm H})$	0.53	0.44	−0.01
	$\log(L_{\rm H,cor})$	0.44	0.39	−0.06
	$\log(L_{\rm S})$	0.45	0.27	−0.01
	$\log(L_{\rm S,cor})$	0.44	0.39	−0.06
Sy1+Sy2	$\log(L_{\rm H})$	0.89	0.82	0.60
	$\log(L_{\rm H,cor})$	0.89	0.82	0.58
	$\log(L_{\rm S})$	0.88	0.80	0.59
	$\log(L_{\rm S,cor})$	0.88	0.82	0.58

Table 4. Summary of the Spearman's rank correlation coefficients, $\rho_{\rm F}$, between the X-ray flux and IR flux density.

		IR flux density		
Type	X-ray flux	$\log(f_9)$	$\log(f_{18})$	$\log(f_{90})$
Sy1	$\log(F_{\rm H})$	0.42	0.39	0.40
	$\log(F_{\rm H,cor})$	0.42	0.39	0.40
	$\log(F_{\rm S})$	0.47	0.43	0.42
	$\log(F_{\rm S,cor})$	0.41	0.37	0.39
Sy2	$\log(F_{\rm H})$	0.53	0.19	−0.05
	$\log(F_{\rm H,cor})$	0.46	0.22	−0.01
	$\log(F_{\rm S})$	0.57	0.11	−0.09
	$\log(F_{\rm S,cor})$	0.44	0.23	−0.01
Sy1+Sy2	$\log(F_{\rm H})$	0.42	0.33	0.19
	$\log(F_{\rm H,cor})$	0.47	0.39	0.25
	$\log(F_{\rm S})$	0.34	0.23	0.09
	$\log(F_{\rm S,cor})$	0.46	0.38	0.23

field (Gandhi et al. 2009). Our study successfully complements the previous ones, because the sample originates in the relatively unbiased all-sky X-ray survey below 10 keV, conducted by MAXI with the highest sensitivity.

Figures 8 and 9 suggest that the dispersion of the ratio between the X-ray luminosity to the far-IR one L_{90} ($\sigma_{\rm r} \simeq 0.4$ for the Sy1 galaxies) is slightly larger than those to the mid-IR ones, L_9 and L_{18} ($\sigma_{\rm r} \simeq 0.3$). In relation, the X-ray correlation coefficients to $\log(L_{90})$ tends to be smaller than those to $\log(L_9)$ and $\log(L_{18})$. It is pointed out that within the AKARI angular resolution non-negligible contribution to the far-IR emission from warm dust related to star formation activity in the host galaxy resulted in this larger scatter and lower correlation coefficients at 90 μm (Matsuta et al. 2012).

4.3 Behavior of Compton-thick objects

Interestingly, we found an outlier on figures 8 and 9, which is located significantly outside the $2\sigma_{\rm r}$ region of the Sy1 galaxies. This object, indicated with the red open triangles in figure 8, is NGC 1365. Although this source is optically classified as Sy1.8, it is known to exhibit occasionally a Compton-thick X-ray spectrum with $N_{\rm H} > 10^{24}$ cm^{-2} (e.g., Risaliti et al. 2005; Risaliti et al. 2007; Risaliti et al. 2009a; Risaliti et al. 2009b).

A standard population synthesis model by Ueda et al. (2014) which was constructed from the X-ray luminosity function of active galactic nuclei to reproduce the X-ray background spectrum predicts the fraction of the Compton-thick objects as $< 1\%$ and $\sim 6\%$ in the 2–10 keV and 10–40 keV bands, respectively, at the flux limit of our sample. The observed Compton-thick fraction (i.e., 1 out of 100) is in a reasonable agreement with these predictions, given the fact that our sample is essentially selected by MAXI and the Swift/BAT (see §2.1) with an energy coverage of 4–10 keV and 14–195 keV, respectively, which well overlaps with the energy bands considered in Ueda et al. (2014).

X-ray spectrum below 10 keV of Compton-thick Seyfert galaxies is not dominated by the direct/absorbed emission from their nucleus. Instead, their dominant spectral component in this X-ray band is though to be reflected and/or scattered ones (e.g., Gilli et al. 2007; Ueda et al. 2014). As a result, Compton-thick objects are possible to exhibit a relatively soft X-ray spectrum, in comparison to Compton-thin Sy2 galaxies with a moderate column density (e.g., $N_{\rm H} = 10^{22} - 10^{23}$ cm^{-2}). The X-ray luminosity below 10 keV of the reflected/scattered component is estimated to be by typically an order of magnitude less than the unabsorbed luminosity of the direct component. Therefore, for the Compton-thick sources, the absorption correction based on the HR–$N_{\rm H}$ relation in figure 7 should yield a column density lower than the real value, and thus, significantly underestimates their intrinsic luminosity. Using the hard X-ray catalog with Swift/BAT of nearby Seyfert galaxies, Matsuta et al. (2012) reported a sign of a deficit in the hard X-ray luminosity from Compton-thick sources.

The hardness ratio, $HR = 0.07 \pm 0.07$, of NGC 1365 is within the range of those of the Sy1 galaxies, and thus indicates a soft X-ray spectrum in the MAXI energy range. This HR value corresponds to a low column density of $N_{\rm H} \sim 4 \times 10^{21}$ cm^{-2} (in the case of $\Gamma = 1.9$), in spite of its Sy2 nature. The X-ray-to-IR luminosity ratio of NGC 1365 after the absorption correction is by a factor of $\gtrsim 10$ lower than the average value of the Sy1 galaxies, as shown in figure 8. These two observational facts seem suggestive of the Compton-thick picture for NGC 1365.

From recent studies (Severgnini et al. 2015; Terashima et al. 2015), the relation between the observed X-ray hardness and X-ray-to-IR color is proposed as an effective tool to pick up Compton-thick active galactic nuclei. In panels (a) and (b) of figure 10, we plot HR against the absorption-inclusive values of $\log(L_{\rm H}/L_{18})$ and $\log(L_{\rm S}/L_{18})$, respectively, for the 2MAXI-AKARI sample. On these diagrams, the model prediction is plotted as a function of $N_{\rm H}$ (from 0 to 1×10^{25} cm^{-2}) with

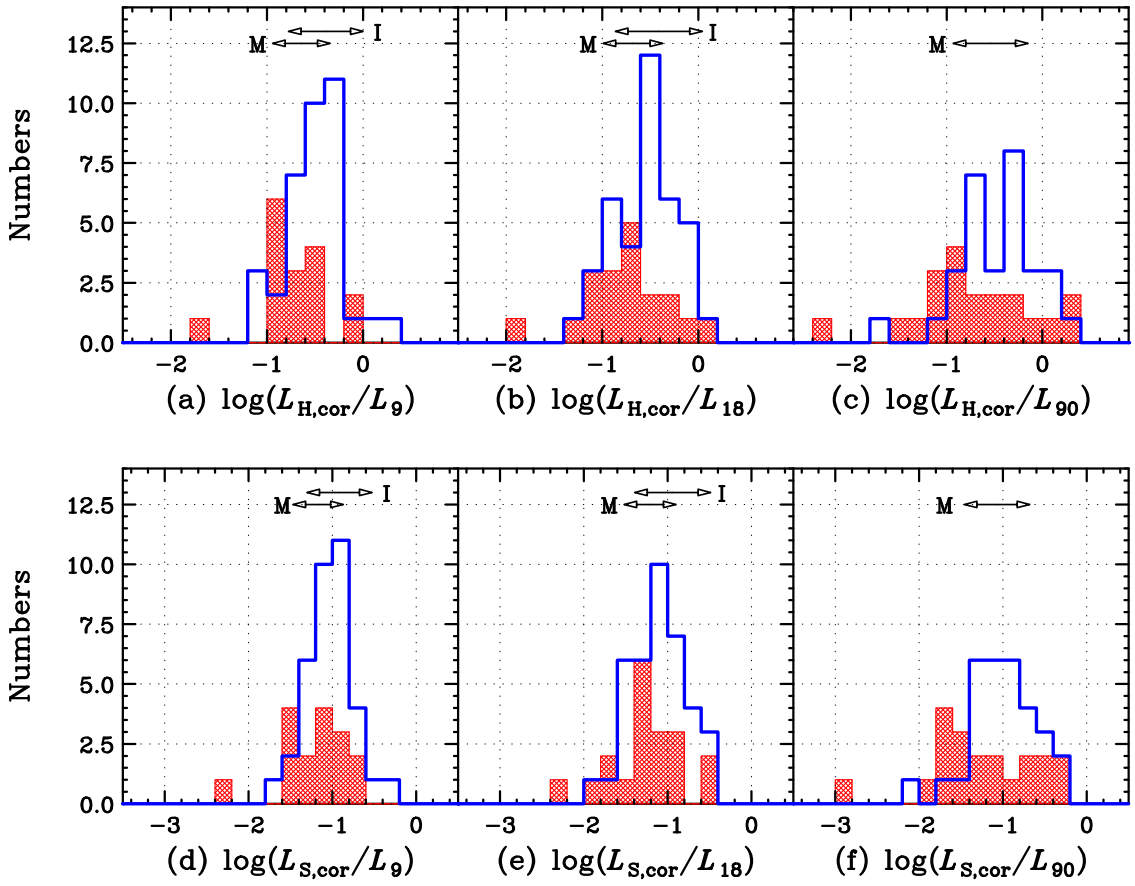

Fig. 9. Distributions of the logarithmic ratio between the X-ray and IR luminosities, after the X-ray absorption correction; (a) $\log(L_{\rm H,cor}/L_9)$, (b) $\log(L_{\rm H,cor}/L_{18})$, (c) $\log(L_{\rm H,cor}/L_{90})$, (d) $\log(L_{\rm S,cor}/L_9)$, (e) $\log(L_{\rm S,cor}/L_{18})$, and (f) $\log(L_{\rm S,cor}/L_{90})$ The distributions among the Sy1 and Sy2 galaxies are indicated with the thick blue and hatched red histograms respectively. The $1\sigma_{\rm r}$ range of the luminosity ratio for the Sy1 galaxies estimated from Matsuta et al. (2012) and Ichikawa et al. (2012) are shown with the horizontal arrows indicated as "M" and "I", respectively.

the dotted lines. The dashed lines indicate the absorption column of $N_{\rm H} = 4 \times 10^{23}$, 1×10^{24}, 2×10^{24}, and 4×10^{24} cm^{-2}. By referring to Terashima et al. (2015), we introduced to the absorbed power-law model, an additional unabsorbed power-law one which represents the reflected/scattered component. The photon index of the reflected/scattered component was presumed to be identical to the direct one (i.e., $\Gamma = 1.9$; see §4.1). We evaluated the model tracks, by assuming the fraction of the scattered/reflected component as 1%, 2%, 5%, and 10% to the intrinsic luminosity of the direct component. The $\log(L_{\rm H}/L_{18})$ and $\log(L_{\rm S}/L_{18})$ values of a source unaffected by absorption (i.e., $N_{\rm H} = 0$) were assumed to be their mean among Sy1 galaxies (i.e., represented by the solid lines in figure 3).

In the Compton-thin regime ($N_{\rm H} < 10^{24}$ cm^{-2}), a source with a higher $N_{\rm H}$ value is expected to exhibit a harder X-ray spectrum and a lower ratio of the soft X-ray to IR luminosities. In contrast, the hard-X-ray to IR color is relatively insensitive to the absorption. For heavily obscured objects, an $N_{\rm H}$ increase is predicted to result in a significant X-ray spectral softening and a decrease in $\log(L_{\rm H}/L_{18})$. The $\log(L_{\rm S}/L_{18})$ value is inferred to remain unchanged because the direct X-ray emission in the soft band has been fully blocked by the Compton-thick dust torus, and hence, is totally dominated by the scattered/reflected component. We clearly recognize in figure 10 that the behavior of the 2MAXI-AKARI Seyfert galaxies, qualitatively follows these trends. Especially, we can explain the colors of NGC 1365 by tuning the fraction of the scattered/reflected component and the X-ray-to-IR luminosity ratio for $N_{\rm H} = 0$, both of which are thought to reflect the geometry of the dust torus around the accretion disk. We have, thus, re-confirmed that a combination of the X-ray spectral hardness below 10 keV and the X-ray-to-IR color is useful to distinguish the Compton-thick sources from the Compton-thin ones, without any detailed spectral analysis, or hard X-ray data above 10 keV.

Finally, it is important to mention that figure 10 implies a few additional Compton-thick candidates, which are located in

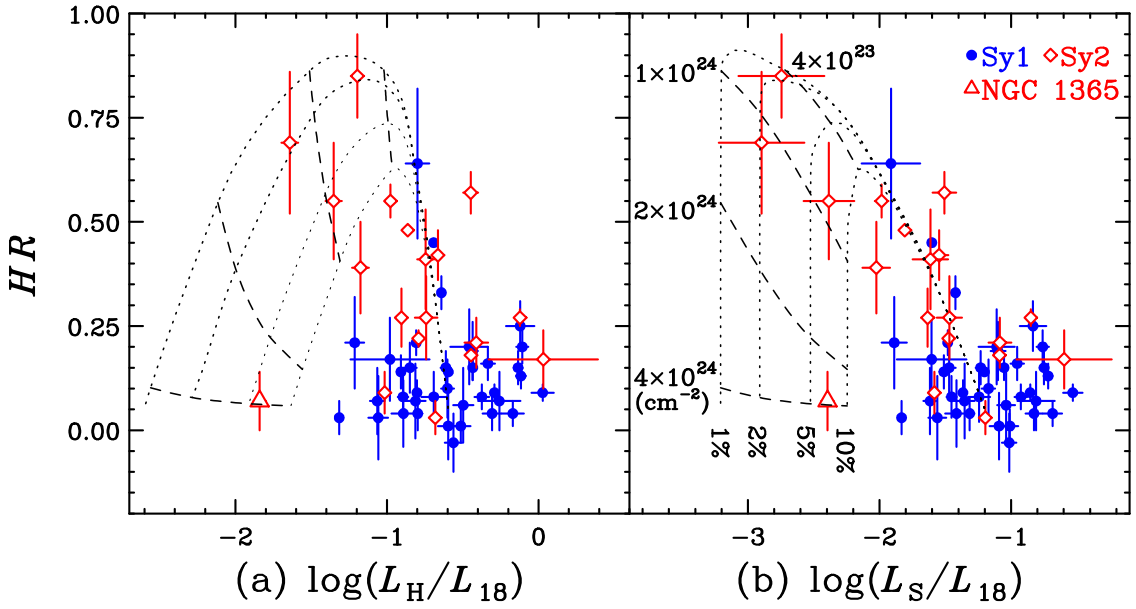

Fig. 10. X-ray hardness ratio HR is plotted against the logarithm of the absorption-inclusive X-ray to IR luminosity ratios, $\log(L_{\rm H}/L_{18})$ and $\log(L_{\rm S}/L_{18})$, in panels (a) and (b) respectively. The blue filled circles and red open diamonds shows the Sy1 and Sy2 galaxies, respectively, while the red open triangle indicates NGC 1365. The model prediction estimated for some representative values of the fraction of the scattered component (1%, 2%, 5% and 10%) are drawn with the dotted lines, where the $\log(L_{\rm H}/L_{18})$ and $\log(L_{\rm S}/L_{18})$ values for a source with no absorption ($N_{\rm H} = 0$) are simply assumed to be their average over the Sy1 galaxies in the sample. The dashed lines indicate the absorption column density of $N_{\rm H} = 4 \times 10^{23}$, 1×10^{24}, 2×10^{24}, and 4×10^{24} cm^{-2}.

the transition area between the Compton-thin and -thick objects, represented by $\log(L_{\rm H}/L_{18}) \lesssim -1$ or $\log(L_{\rm S}/L_{18}) \lesssim -2$ (corresponding to $N_{\rm H} > 4 \times 10^{23}$ cm^{-2}). Detailed X-ray spectral analyses are considered to be required to find out the nature of these objects (e.g., Terashima et al. 2015), although we regard them as out of the scope of the present paper.

4.4 Implication from the IR color

The mid-IR spectrum of Seyfert galaxies is utilized as a good probe into physical or geometrical properties of their dust torus, because it is known to be dominated by emission from the dust torus especially in the $10-20$ μm range (Mor et al. 2009). It is pointed out that the $5-20$ μm IR spectra of nearby Sy2 galaxies are possibly redder than those of the Sy1 objects (e.g., Mateos et al. 2016). Based on the numerical simulation on the clumpy torus model (e.g., Nenkova et al. 2008a; Nenkova et al. 2008b), these spectral characteristics are proposed to be explained by a possible idea that the covering factor of the dust torus is larger in the Sy2 sources than in the Sy1 ones (Mateos et al. 2016). However, our result shown in the left panel of figure 6 does not seem to give a support to such a scenario, since no clear discrepancies are found between the Sy1 and Sy2 sources.

As briefly mentioned in §4.2, the far-IR luminosity from the Seyfert galaxies measured with AKARI is thought to be rather contaminated by emission from warm dust produced by star-forming activity in their host galaxy. Then, the mid-to-far IR luminosity ratio is regarded as an indicator of a relative dominance between the activities of the nucleus and star formation in the galaxies. Using the AKARI data for the Swift/BAT sample, Matsuta et al. (2012) hinted a higher relative star formation activity in the Sy2 galaxies, based on their redder L_9/L_{90} color, in comparison to the Sy1 objects. We reconfirmed this trend (with a probability of $\sim 95\%$ by the K-S test), by utilizing the 2MAXI-AKARI sample, as shown in the right panel of figure 6. In addition, no meaningful X-ray correlation to $\log(L_{90})$ indicated to the Sy2 galaxies (see tables 3 and 4) is possible to be also related to a significant contamination from a higher star-formation activity in such objects. These results suggest that the optical Seyfert classification is not only determined by the orientation of the dust torus to our line of sight, but also by the warm-dust distribution connected to the star-forming activity in the host galaxy.

Acknowledgments

We thank the anonymous referee for her/his supportive comments to modify the present paper. This research is financially supported by the Ministry of Education, Culture, Sports, Science and Technology (MEXT) of Japan, through the Grant-in-Aid 24103002 (N.I.), 26247030 (T.N.) and 26400228 (Y.U.). T.K. is supported by the Grant-in-Aid for JSPS Fellows. We made use of the MAXI catalog (Hiroi et al. 2013), which was constructed from the MAXI data provided by RIKEN, JAXA and the MAXI team. This work is based on the data taken with AKARI, a JAXA project, with the participation of ESA. In advance of publication, Dr. Ichikawa kindly provided us with the IR data of the Swift/BAT sample.

References

Antonucci, R., 1993, ARA&A, 31, 473
Baumgartner, W. H., et al. 2013, ApJS, 207, 19
Burlon, D., et al. 2011, ApJ, 728, 58
Elitzur, M., 2008, New Astron., 52, 274
Elvis, M., et al. 1994, ApJS, 95, 1
Fürst, F., et al. 2016, ApJ, accepted (arXiv:1511.01915)
Gandhi, P., et al. 2009, A&A, 502, 457
Gilli, R., Comastri, A. & Hasinger, G., 2007, A&A, 463, 79G
Hiroi, K., et al. 2011, PASJ, 63, S677
Hiroi, K., et al. 2013, ApJS, 207, 36
Ichikawa, K., et al. 2012, ApJ, 754, 45
Ishihara, D., et al. 2010, A&A, 514, A1
Isobe, N., et al. 2010, PASJ, 62, L55
Isobe, N., et al. 2015, ApJ, 798, 27
Kawada, M., et al. 2007, PASJ, 59, S389
Kirsch, M. G., et al. 2005, SPIE, 5898, 22
Krolik, J. H., & Begelman, M. C., 1988, ApJ, 329,702
Markowitz, A., et al. 2007, ApJ, 665, 209
Mateos, S., et al. 2016, ApJ, accepted (arXiv:1601.04439)
Matsuoka, M., et al. 2009, PASJ, 61, 999
Matsuta, K., et al. 2012, ApJ, 753, 104
Mihara, T., et al., 2011, PASJ, 63, S623
Mitsuda, K., et al. 2007, PASJ, 5Suzaku9, S1
Mor, R., Netzer, H., & Elitzur, M., 2009, ApJ, 705, 298
Murakami, H., et al. 2007, PASJ, 59, S369
Nenkova, M., et al. 2008b, ApJ, 685, 147
Nenkova, M., 2008, ApJ, 685, 160
Onaka, T., et al. 2007, PASJ, 59, S401
Piffaretti, R., et al. 2011, A&A, 534, 109
Pier, E. A., & Krolik, J. H., 1993, ApJ, 18, 673
Risaliti, G., et al. 2005, ApJ, 623, L93
Risaliti, G., et al. 2007, ApJ, 659, L111
Risaliti, G., et al. 2009a, MNRAS, 393, L1
Risaliti, G., et al. 2009b, ApJ, 705, L1
Sanders, D. B., Phinney, E. S., Neugebauer, G., Soifer, B. T., & Matthews, K., 1989, ApJ, 347, 29 1989ApJ...347...29S
Severgnini, P., et al. 2012, A&A, 542, A46
Sugizaki, M., et al. 2011, PASJ, 63, S635
Sunyaev, R. A., & Titarchuk, L. G., 1980, A&A, 86, 121
Tachibana, Y., et al. 2016, PASJ, accepted (arXiv:1504.03208)
Terashima, Y., et al. 2015, ApJ, 814, 11
Yamamura, I., et al. 2012, Publications of The Korean Astronomical Society, 27, 105
Yamauchi, C., et al. 2011, PASP, 123, 852
Ueda, Y., et al. 2007, ApJ, 664, L79
Ueda, Y., et al. 2014, ApJ, 786, 104
Ueda, Y., et al. 2011, PASJ, 63, S937
Urry, C. M., & Padovani, P., 1995, PASP, 107, 803